© 2017. Published by The Company of Biologists Ltd | Development (2017) 144, 2694-2701 doi:10.1242/dev.150094

A toolkit for GFP-mediated tissue-specific protein degradation in *C. elegans*

Shaohe Wang[1,*], Ngang Heok Tang[2], Pablo Lara-Gonzalez[1], Zhiling Zhao[1], Dhanya K. Cheerambathur[1], Bram Prevo[1], Andrew D. Chisholm[2], Arshad Desai[1] and Karen Oegema[1,‡]

ABSTRACT

Proteins that are essential for embryo production, cell division and early embryonic events are frequently reused later in embryogenesis, during organismal development or in the adult. Examining protein function across these different biological contexts requires tissue-specific perturbation. Here, we describe a method that uses expression of a fusion between a GFP-targeting nanobody and a SOCS-box containing ubiquitin ligase adaptor to target GFP-tagged proteins for degradation. When combined with endogenous locus GFP tagging by CRISPR-Cas9 or with rescue of a null mutant with a GFP fusion, this approach enables routine and efficient tissue-specific protein ablation. We show that this approach works in multiple tissues – the epidermis, intestine, body wall muscle, ciliated sensory neurons and touch receptor neurons – where it recapitulates expected loss-of-function mutant phenotypes. The transgene toolkit and the strain set described here will complement existing approaches to enable routine analysis of the tissue-specific roles of *C. elegans* proteins.

KEY WORDS: Protein degradation, *C. elegans*, ZIF-1, GFP nanobody, vhhGFP4

INTRODUCTION

Techniques for disrupting protein function in specific tissues or at particular points in development are enabling detailed analysis of developmental mechanisms. To enable tissue-specific perturbation of gene function in *C. elegans*, methods for Cre-lox-, FLP-FRT- and CRISPR-Cas9-based gene knockouts, as well as tissue-specific RNAi have been described previously (Hubbard, 2014; Qadota et al., 2007; Shen et al., 2014). However, the utility of DNA/RNA-editing approaches can be limited by perdurance of the target protein following excision, which can delay the manifestation of phenotypes.

An alternative approach that circumvents this problem is to directly target proteins for degradation in specific tissues. One method for achieving this that was recently adapted for *C. elegans* (Zhang et al., 2015) is based on transplanting the auxin-induced protein degradation system from plants (Holland et al., 2012; Nishimura et al., 2009). In this system, addition of the small molecule auxin activates a plant-specific F-box protein, TIR1, that serves as a substrate recognition component for a Skp1–Cullin–F-box (SCF) E3 ubiquitin ligase. Active TIR1 targets proteins containing a specific degron sequence. However, a robust genetically encoded method that does not require a small molecule would also be useful, as the exposure kinetics and dose of small molecules in *C. elegans* is limited by barriers such as the cuticle and the eggshell. To this end, a method was developed that takes advantage of an endogenous *C. elegans* protein degradation system. With this approach, target proteins are tagged with a 36 amino acid degron sequence (ZF1); the SOCS-box adaptor protein ZIF-1, which targets ZF1-containing proteins for proteasomal degradation, is expressed in the target tissue (Armenti et al., 2014). However, a limitation of this system is that ZIF-1 plays an essential role during early embryogenesis (DeRenzo et al., 2003; Reese et al., 2000). Thus, proteins tagged with the ZF1 degron are degraded during embryogenesis as well as in the target tissue, which is problematic for analysis of proteins that function during embryogenesis as well as at later developmental stages. More recently, a bacterial sortase-based protein ligation approach was also used to achieve targeted protein degradation in *C. elegans* (Wu et al., 2017). This approach requires tagging the target protein with a small five amino acid tag and expressing a tagged F-box along with a modified sortase.

Here, we have developed a new system that combines potent ZIF-1-mediated protein degradation (Armenti et al., 2014) with the previously described deGradFP approach (Caussinus et al., 2012). In deGradFP, a GFP nanobody is fused to a F-box protein to degrade GFP-tagged proteins. As neither the originally described F-box adaptor nor the *C. elegans* LIN-23 F-box works in *C. elegans* (S.W. and K.O., unpublished), we fused the GFP nanobody to ZIF-1. We show that expression of this fusion enables efficient depletion of GFP-tagged proteins across multiple tissues. In conjunction with GFP tagging at endogenous loci using CRISPR-Cas9 (Paix et al., 2016) or rescue of null mutants with GFP fusions expressed from transgenes, this approach enables routine protein depletion controlled by the spatial and temporal expression pattern of the promoter driving the GFP-degrading module. We describe a toolkit of transgenes expressing GFP degradation adaptors in different tissues that should facilitate tissue-specific analysis of protein function in *C. elegans*.

RESULTS

Epidermal expression of a GFP nanobody::ZIF-1 fusion depletes GFP-tagged proteins that localize to different subcellular locations

To selectively degrade GFP-tagged proteins, we expressed a GFP nanobody::ZIF-1 fusion under different tissue-specific promoters (Fig. 1A). This fusion acts as a GFP-to-ligase adapter that promotes

[1]Ludwig Institute for Cancer Research, Department of Cellular and Molecular Medicine, University of California San Diego, La Jolla, CA 92093, USA. [2]Section of Neurobiology, Division of Biological Sciences, University of California San Diego, La Jolla, CA 92093, USA.
*Present address: Cell Biology Section, National Institute of Dental and Craniofacial Research, National Institutes of Health, Bethesda, MD 20892, USA.

‡Author for correspondence (koegema@ucsd.edu)

S.W., 0000-0001-9522-2359; N.H.T., 0000-0002-0977-0816; K.O., 0000-0001-8515-7514

Received 30 January 2017; Accepted 8 June 2017

Development (2017) 144, 2694-2701 doi:10.1242/dev.150094

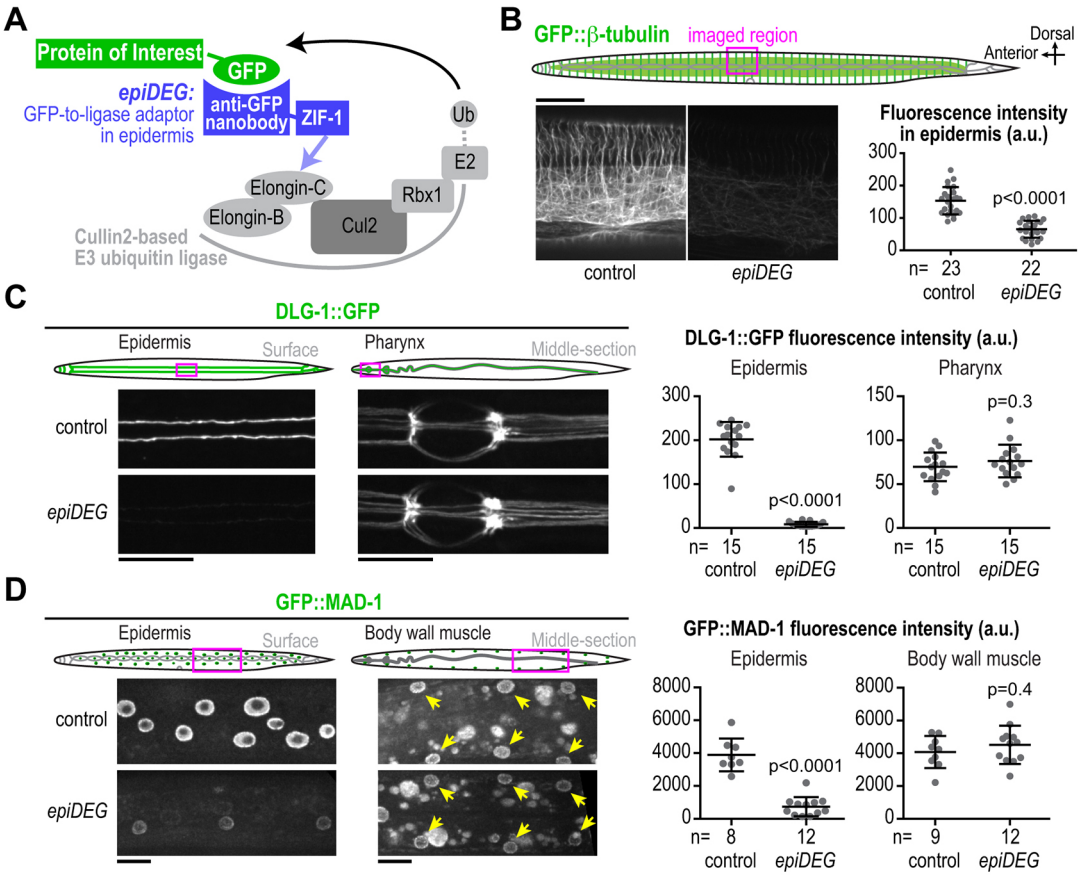

Fig. 1. *epiDEG* efficiently degrades GFP-tagged proteins that localize to different subcellular localizations. (A) Schematic illustrating the method. (B) Top: schematic showing imaged region. Bottom: fluorescence confocal images of L3 stage worms expressing GFP::β-tubulin and plots of GFP::β-tubulin fluorescence intensity. (C) Left: schematics and fluorescence confocal images of late L4 stage worms expressing DLG-1::GFP. Right: plots of DLG-1::GFP fluorescence intensity. (D) Left: schematics and fluorescence confocal images of L3 stage worms expressing GFP::MAD-1. Yellow arrows indicate the body wall muscle nuclei. Right: plots of GFP::MAD-1 fluorescence intensity. *n* is the number of worms analyzed. Data were analyzed using a two-tailed Student's *t*-test. *P* values are the probability of obtaining the observed results assuming the test group is the same as control. Data are shown as mean±s.d. Scale bars: 10 µm.

ubiquitylation of the GFP-tagged protein by the Cul2 family E3 ligase CUL-2 and its subsequent degradation by the proteasome (DeRenzo et al., 2003). We have previously shown that epidermis-specific expression of a GFP nanobody::ZIF-1 fusion (*epiDEG;* Fig. 1A) led to efficient degradation of an endogenously tagged GFP fusion with the γ-tubulin complex component GIP-2 (Wang et al., 2015). To test whether *epiDEG* can target proteins that localize to different subcellular locations, we crossed the *epiDEG* transgene into strains expressing GFP-tagged proteins that localize to: the cytoplasm (transgene-encoded GFP::β-tubulin expressed using the *dpy-7* promoter; Fig. 1B), apical cell junctions (transgene-encoded DLG-1::GFP expressed using the *dlg-1Δ7* promoter; Fig. 1C), and the nucleus and nuclear envelope [*in situ*-tagged GFP::MAD-1 (also called MDF-1 in the *C. elegans* literature); Fig. 1D]. Quantification (Fig. S1A-C) revealed a striking reduction in GFP fluorescence intensity in the larval epidermis for all three markers (DLG-1::GFP, 96%; GFP::MAD-1, 81%; GFP::β-tubulin, 58%; Fig. 1B-D), whereas signal intensity was unchanged in control tissues (Fig. 1C,D; DLG-1::GFP and GFP::MAD-1, GFP::β-tubulin was expressed in the epidermis only). We conclude that the GFP nanobody::ZIF-1 fusion can degrade proteins that localize to different subcellular locations; we note that it remains unclear whether depletion of proteins from the nucleus and cellular junctions occurs by targeting and degradation at these locations or by degrading the protein from the cytoplasm. With the exception of GFP::β-tubulin, which we expect is heavily expressed, reduction by *epiDEG* was consistently greater than 80% (Fig. 1C,D; Wang et al., 2015).

GFP-mediated protein degradation is efficient in multiple *C. elegans* tissues

To determine whether the GFP nanobody::ZIF-1 fusion could degrade GFP-tagged proteins in different tissues, we expressed the GFP nanobody::ZIF-1 fusion or ZIF-1 alone (as a control) using promoters that drive expression in the intestine (*intDEG*, P*elt-2*; Fukushige et al., 1998), body wall muscle (*bwmDEG*, P*myo-3*; Fire and Waterston, 1989) and ciliated sensory neurons (*csnDEG*, P*osm-6*; Collet et al., 1998). The transgenes also included an operon linker (Huang et al., 2001) followed by an mCherry::Histone H2b reporter to allow identification of cells expressing the degradation module (*DEG*) or control transgenes (Fig. 2A). To assess the relative function of the degradation module in different tissues, the transgenes were introduced into a background expressing *in situ*-tagged GFP::MAD-1, which localizes to nuclei across differentiated tissues throughout development (Fig. S2A,B). In all three tested tissues, GFP::MAD-1 signal was eliminated when the GFP nanobody::ZIF-1 fusion, but not ZIF-1 alone, was expressed (Fig. 2B-D). We conclude that the GFP nanobody::ZIF-1 fusion targets GFP-tagged proteins for degradation in multiple tissues (promoters and targets are summarized in Table S1; an analysis

Development (2017) 144, 2694-2701 doi:10.1242/dev.150094

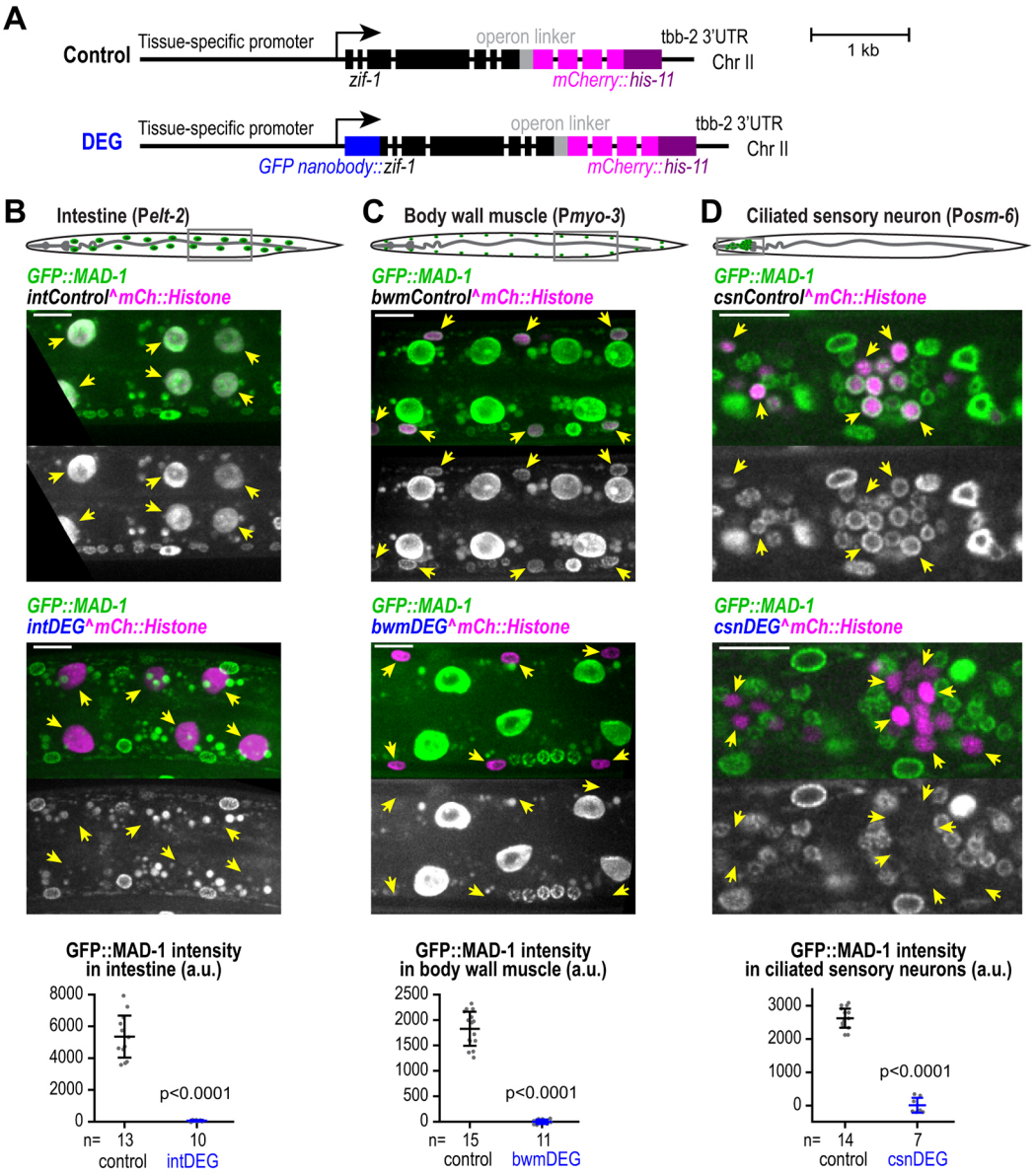

Fig. 2. GFP-mediated protein degradation is efficient in multiple *C. elegans* tissues. (A) Transgene schematics. (B-D) Top: schematics showing imaged region. Middle: fluorescence confocal images (maximum intensity projections in B and C, single *z*-slice in D) of L3 stage worms expressing GFP::MAD-1. Yellow arrows indicate nuclei. Bottom: plots of GFP::MAD-1 fluorescence intensity. *n* is the number of worms analyzed. Each data point in B and C represents an average of five nuclei from the same worm. Data were analyzed using a two-tailed Student's *t*-test. *P* values are the probability of obtaining the observed results assuming the test group is the same as control. Data are shown as mean±s.d. Scale bars: 10 µm.

of reporter expression showing when each promoter turns on is in Fig. S3).

GFP-mediated protein degradation is rapid and target dependent

Next, we used time lapse imaging to follow degradation kinetics for two *in situ* GFP-tagged target proteins (GFP::MAD-1 and GFP::PP1^{GSP-2}) in the intestine of *C. elegans* embryos, where expression of the nanobody-ZIF-1 fusion is under the control of the *elt-2* promoter (*intDEG*). Degradation kinetics result from a combination of the kinetics with which levels of the nanobody-ZIF-1 fusion increase as the *elt-2* promoter becomes active and the time required for the fusion to shuttle the target for degradation. Thus, we would expect the degradation of more abundant proteins to take longer. Visual inspection suggested that GFP::MAD-1 was degraded within ~12 min (Fig. 3A and Movie 1). Owing to the relatively long folding time for the mCherry fluorophore, the GFP::MAD-1 signal had disappeared ~50 min before the first point where the mCherry::histone signal, which marks nuclei in cells expressing the *intDEG* cassette, could be detected (Fig. 3A and Movie 1). The rapid disappearance of GFP::MAD-1 prior to expression of our mCherry nuclear landmark prevented a more detailed quantification. The second target, GFP::PP1^{GSP-2}, is expressed at ~4-fold higher levels (Fig. 3B) and its cytoplasmic outline allowed us to quantify the signal back to degradation onset prior to appearance of the mCherry histone landmark. As for GFP::MAD-1, degradation of GFP::PP1^{GSP-2} began about 50 min before the point where the mCherry::histone signal first became detectable (Fig. 3C,D and Movie 2). However, in this case, the point when the signal was reduced by ~80% was about 30 min after the mCherry::histone signal first

Development (2017) 144, 2694-2701 doi:10.1242/dev.150094

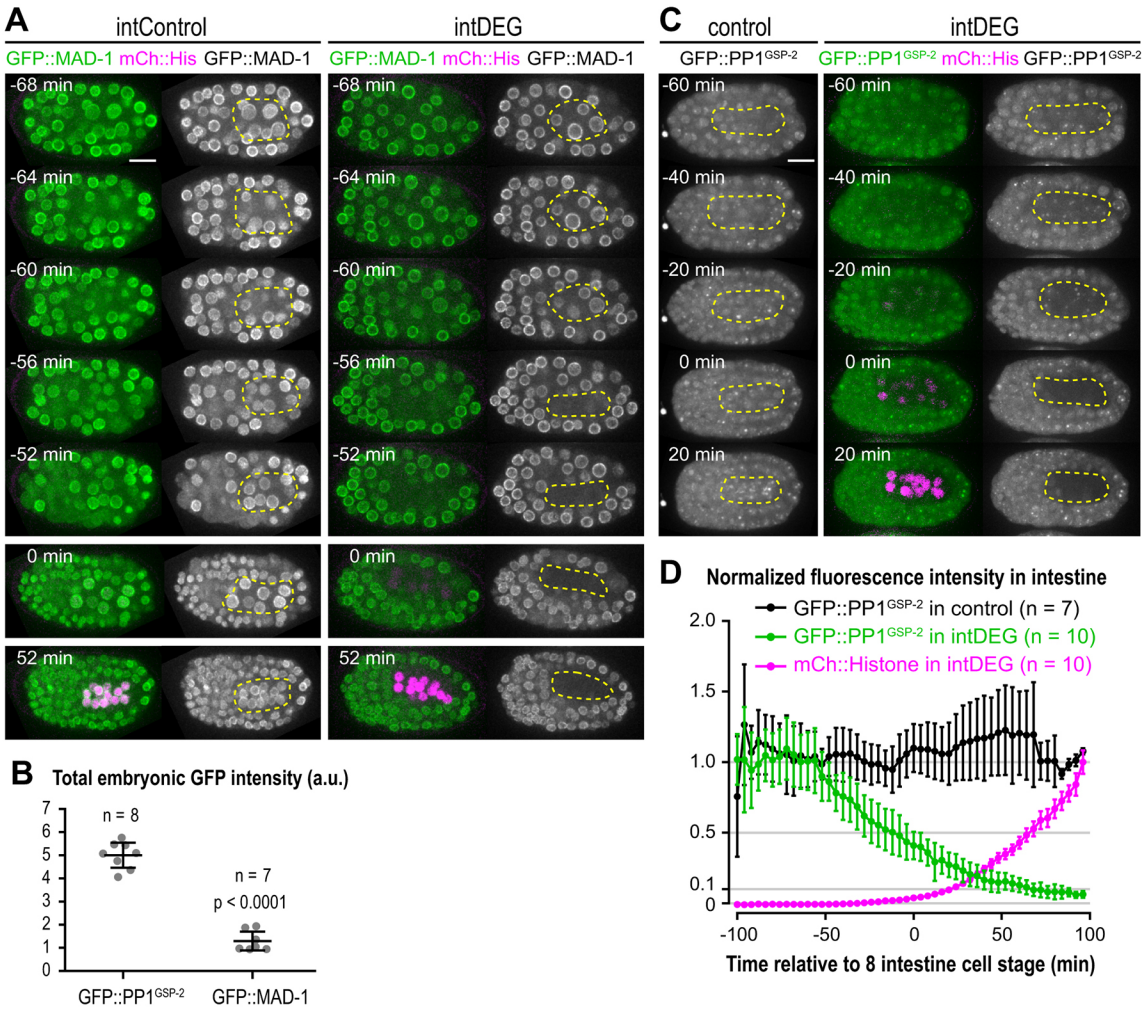

Fig. 3. GFP-mediated protein degradation is rapid in *C. elegans* intestine. (A) Still images from time-lapse confocal imaging of embryos expressing GFP::MAD-1 and either the *intControl* or *intDEG* cassettes (also see Movie 1). (B) Graph quantifying total per embryo GFP fluorescence for GFP::PP1^{GSP-2} and GFP::MAD-1. (C) Still images from time-lapse confocal imaging of control and intDEG embryos expressing GFP::PP1^{GSP-2} (also see Movie 2). Dashed yellow outlines show the location of the intestinal cells in A and C. (D) Plot of normalized GFP::PP1^{GSP-2} or mCherry::histone intensity in control or intDEG embryos. *n* is the number of embryos analyzed. Data are shown as mean±s.d. Scale bars: 10 µm.

became detectable (Fig. 3C,D and Movie 2). We conclude that penetrant degradation of both targets occurs rapidly relative to the time-scale of developmental events. However, the precise timing with which penetrant depletion is achieved following promoter turn-on depends on target-specific features, most likely abundance and/or accessibility.

Degradation of GFP::DLK-1 in the touch receptor neurons blocks axon regeneration

To determine whether GFP-mediated protein degradation could recapitulate loss-of-function phenotypes in the nervous system, we expressed the GFP nanobody::ZIF-1 fusion from a transgene that also included cytoplasmic mKate2 (to visualize axons) in the touch receptor neurons using the *mec-18* promoter (*trnDEG*; Fig. 4A). To assess efficacy, we targeted a GFP fusion with DLK-1 (Dual-Leucine zipper Kinase MAPKKK) (K. Noma and Y. Jin, unpublished), which is required to initiate axon regeneration (Hammarlund et al., 2009; Yan et al., 2009). Following laser-induced axotomy in the PLM touch neuron (Fig. 4B), GFP::DLK-1 promoted axon regrowth in the presence of endogenous DLK-1, consistent with the known effects of DLK-1 overexpression (Hammarlund et al., 2009; Yan et al., 2009), while a *dlk-1* deletion mutant strongly impaired regrowth (Fig. 4C,D). GFP::DLK-1 expression fully rescued the impaired regrowth of the *dlk-1Δ* mutant, and this rescue was abolished by introduction of *trnDEG* (Fig. 4C-E). We note that no defects in axon regrowth were detected in *trnDEG* worms with endogenously tagged GIP-2::GFP or DHC-1::GFP (Fig. S4), suggesting that GIP-2 and DHC-1 are either not expressed or not required for axon regrowth in PLM touch neurons.

Degradation of GIP-2::GFP or PLK-1::sGFP in the intestine causes cell division defects and impairs *C. elegans* growth

To test whether we could use this method to circumvent complications associated with embryonic lethality and observe tissue-specific phenotypes, we analyzed the consequences of depleting two *in situ*-tagged targets, GIP-2::GFP (an essential component of the microtubule-nucleating γ-tubulin complex) and PLK-1::sGFP (fusion of PLK-1, a mitotic kinase that regulates cell cycle progression, with superfolder GFP) in the intestine. The *C. elegans* intestine arises from the E blastomere of the 8-cell embryo (Deppe et al., 1978). The *elt-2* promoter that drives *intDEG* expression turns on at the 2E stage (McGhee et al., 2007) and the

Development (2017) 144, 2694-2701 doi:10.1242/dev.150094

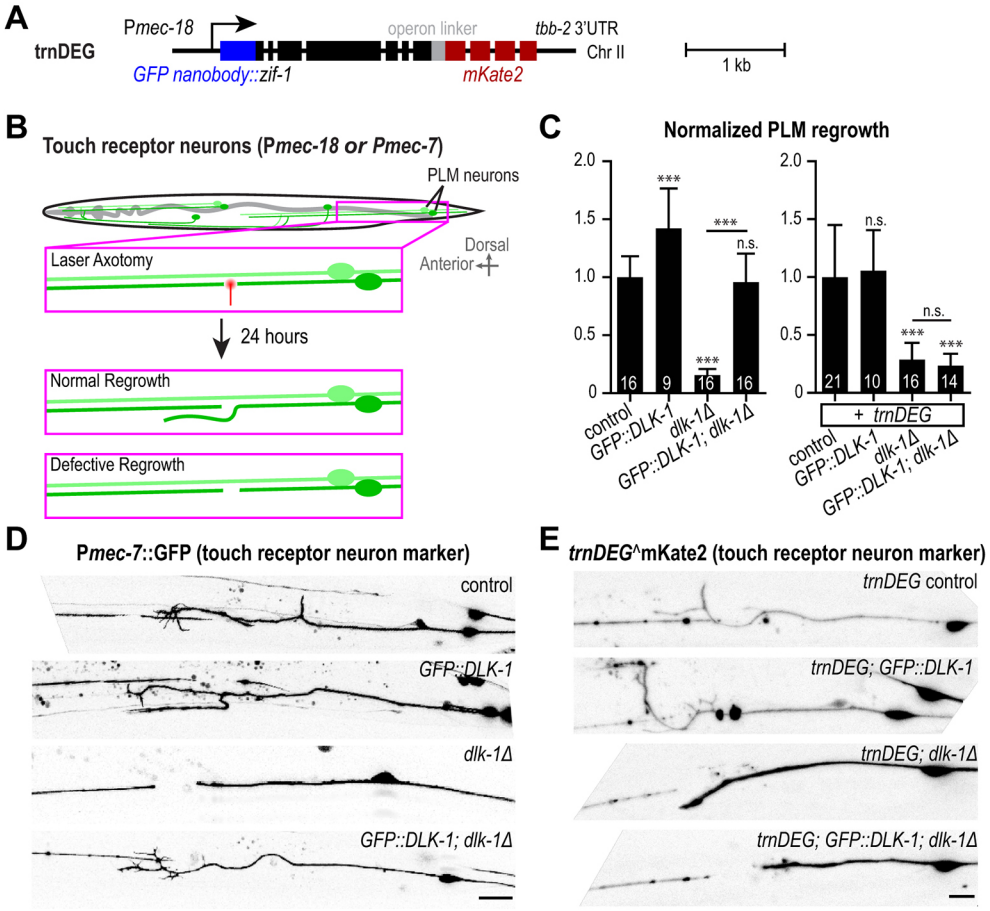

Fig. 4. Degradation of GFP::DLK-1 in the touch receptor neurons blocks axon regeneration. (A) Transgene schematic. (B) Schematic of the axon regeneration assay. (C) Plots of normalized touch neuron (PLM) regrowth at 24 h post laser axotomy. Number in each bar is the number of worms assayed. (D,E) Inverted grayscale images of the touch neuron (PLM) axon. Data were analyzed using a one-way ANOVA with Bonferroni's post test. ***P<0.001. n.s., not significant. Results are compared with control unless specified by the line. Data are shown as mean±s.d. Scale bars: 10 µm.

mCherry::Histone reporter becomes visible at the 8E stage (8-cell intestine; Fig. S3B). During intestinal differentiation in the embryo, the γ-tubulin complex re-localizes from centrosomes to the apical cell surface (Feldman and Priess, 2012; Fig. 5A). Co-expressing *intDEG*, but not the control transgene, eliminated the intestinal GIP-2::GFP and PLK-1::sGFP signals (Fig. 5A-C). As the γ-tubulin complex and PLK-1 are required for cell division (Hannak et al., 2002; Strome et al., 2001), we anticipated that their inhibition might reduce intestinal cell number. Consistent with a cell division defect, in 1.5- to 1.8-fold stage embryos, when control embryos typically have 20 intestinal cells, only 8-15 intestinal nuclei were detected in *intDEG* embryos with *in situ*-tagged GIP-2::GFP or PLK-1::sGFP (Fig. 5D); larval *intDEG* worms also grew more slowly and reached a smaller adult size than controls (Fig. 5E). Thus, intestinal degradation of GIP-2::GFP or PLK-1::sGFP not only resulted in a tissue-specific cell division defect consistent with their known functions, but also revealed a novel post-embryonic developmental defect, demonstrating the utility of the approach.

DISCUSSION

We describe a robust method for the degradation of GFP fusions that complements existing approaches – genetic locus removal, RNA interference, and auxin-, ZF1- and sortase-mediated degradation – to enable tissue-specific analysis of protein function in *C. elegans*. The utility of this approach is enhanced by the recent development of robust CRISPR/Cas9-based methods that enable routine GFP tagging of endogenous loci (Dickinson et al., 2013; Paix et al., 2016). We expect that the set of strains we describe here will be a useful resource to allow the tissue-specific degradation of this emerging collection of *in situ*-tagged proteins and will serve as a template for engineering additional versions that will expand the utility of this strategy.

In principle, degradation kinetics will be influenced by the strength of promoter driving the degron cassette, the efficiency of CUL-2-dependent proteasomal degradation in the target tissue, and target abundance and/or accessibility. An analysis of degradation kinetics for two *in situ*-tagged targets, GFP::MAD-1 and GFP::PP1^{GSP-2}, in the embryonic intestine revealed that GFP::MAD-1 was degraded with a half-life of ∼6 min, whereas GFP::PP1^{GSP-2}, which is more abundant and cytoplasmic/nucleolar rather than nuclear, was degraded with an ∼40 min half-life. These degradation rates are comparable with rates published previously for ZF1 degron-tagged fusions targeted by ZIF-1 expression (15-30 min half-life; Armenti et al., 2014), auxin-inducible degradation (∼20 min half-life; Zhang et al., 2015) and sortase-based F-box ligation-mediated degradation (∼1 h half-life; Wu et al., 2017). Thus, degradation rates will differ between targets depending on abundance and accessibility, but are likely to be comparable for the different methods.

Of the described methods for conditional protein degradation in *C. elegans* (this report; Armenti et al., 2014; Wu et al., 2017; Zhang et al., 2015), each has advantages and limitations. The auxin-inducible degron enables simultaneous spatial (via tissue-specific expression of the TIR1 adaptor) and temporal (timing of auxin addition) control. However, this system requires tagging of the target with the AID degron and auxin addition as well as expression of the TIR1 adaptor in the target tissue. The sortase-based method uses the smallest tag (only 5 amino acids), which could minimize interference with protein function; however, degradation appears to be somewhat

Development (2017) 144, 2694-2701 doi:10.1242/dev.150094

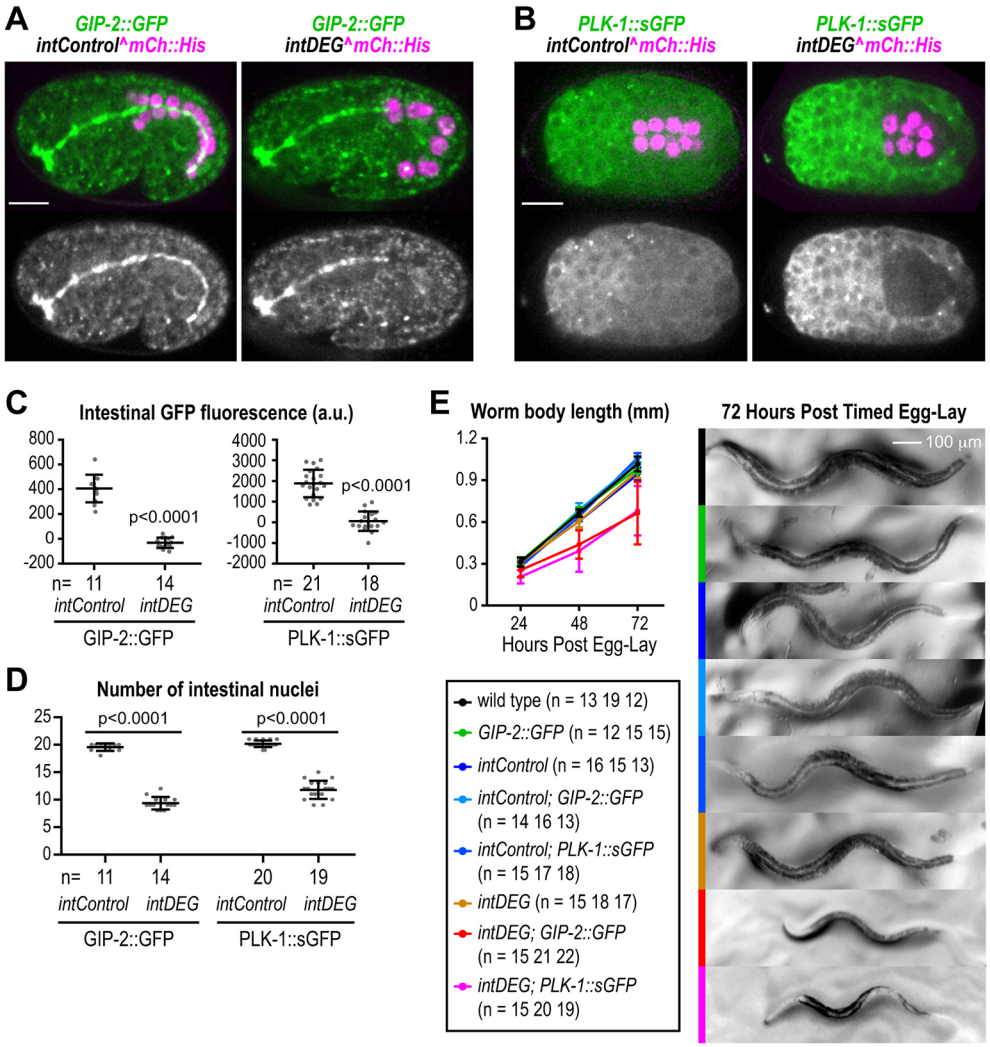

Fig. 5. Degradation of GIP-2::GFP or PLK-1::sGFP in the intestine causes cell division defects and impairs growth. (A) Maximum intensity projections of confocal images of 1.5-fold *C. elegans* embryos expressing GIP-2::GFP with the *intControl* or *intDEG* cassettes. (B) Confocal images of pre-comma *C. elegans* embryos expressing PLK-1::sGFP with the *intControl* or *intDEG* cassettes. (C) Plots of intestinal GFP fluorescence for GIP-2::GFP in 1.5- to 1.8-fold embryos (left) and PLK-1::sGFP in pre-comma embryos (right). *n* is the number of embryos analyzed. (D) Plot of the number of intestinal nuclei in 1.5- to 1.8-fold embryos. *n* is the number of embryos analyzed. (E) Left: plot of body length for worms of the indicated genotypes. Right: representative images of worms at 72 h post timed egg-lay. *n* is the number of worms analyzed at 24, 48 and 72 h. Data were analyzed using a two-tailed Student's *t*-test. *P* values are the probability of obtaining the observed results, assuming the test group is the same as control. Data are shown as mean±s.d. Scale bars: 10 µm (or as indicated).

slower with lower penetrance. Both the 36 amino acid ZF1 degron (Armenti et al., 2014) and the 44 amino acid AID (Zhang et al., 2015) tags are significantly smaller than GFP (238 amino acids) and thus less likely to interfere with protein function. However, since having a fluorescent tag on the target protein is useful for monitoring its degradation, most reported ZF1 and AID degrons to date have been added in conjunction with a GFP tag (Armenti et al., 2014; Zhang et al., 2015). As the CRISPR-Cas9-mediated knock-in method becomes increasingly popular, *in situ* tagging with GFP to enable monitoring of protein localization is likely to become commonplace, and an advantage of our method is that it will allow tissue-specific degradation of these proteins, without any additional engineering, by simply crossing in the transgene that expresses the GFP nanobody::ZIF-1 fusion in the tissue of interest.

A potential concern for both the GFP- and ZF1-mediated degradation methods is that ectopic expression of ZIF-1 or the GFP nanobody::ZIF-1 fusion could lead to off-target effects. Endogenous ZIF-1 is transiently expressed in somatic cells to remove some germline-specific proteins (e.g. PIE-1; DeRenzo et al., 2003). Consistent with the idea that its natural targets are limited to the germline, expressing ZIF-1 in all somatic tissues using a *cdc-42* promoter (Armenti et al., 2014) or the GFP nanobody::ZIF-1 fusion in five different somatic tissues (our data) has not led to any obvious developmental defects. Therefore, ZIF-1-based protein degradation approaches are likely compatible with all somatic tissues. However, as ZIF-1 naturally targets proteins, including PIE-1, that function in the germline, methods that rely on expression of ZIF-1 (Armenti et al., 2014) or a GFP nanobody::ZIF-1 fusion (this report) are likely incompatible with use in the germline.

The GFP nanobody we use here (vhhGFP4; Rothbauer et al., 2006) recognizes common GFP variants such as EGFP, Venus, YFP, EYFP (Caussinus et al., 2012) and superfolder GFP (Fig. 5B,C), but not coral-derived red fluorescent proteins. We have preliminary data that the nanobody also does not recognize mNeonGreen (D.K.C., unpublished), a lancelet-derived green fluorescent protein distantly related to Aequorea GFP (Shaner et al., 2013) that exhibits robust fluorescence in *C. elegans* (Dickinson et al., 2015). Thus, red fluorescent proteins are a good choice for marker fusions for phenotypic analysis in the presence of the degron; mNeonGreen could also be used in cases where it is not necessary to use the green channel to monitor degradation of the tagged GFP fusion.

MATERIALS AND METHODS

C. elegans strains

C. elegans strains (listed in the supplemental Materials and Methods) were maintained at 20°C. Transgenic strains were engineered as described previously (Dickinson et al., 2013; Frøkjær-Jensen et al., 2008). Briefly, GFP or sGFP was fused to the N terminus of MAD-1 and PP1^{GSP-2}, and the C terminus of GIP-2, PLK-1 and DHC-1 at their endogenous loci using CRISPR-Cas9 (Dickinson et al., 2013). Transgenes encoding C-terminally

Development (2017) 144, 2694-2701 doi:10.1242/dev.150094

tagged DLG-1::GFP, N-terminally tagged GFP::β-tubulin^{TBB-2} and GFP::DLK-1 were generated using Mos1 transposon-mediated single-copy insertion (Frøkjær-Jensen et al., 2008). The DEG transgenic strains will be made available through the *Caenorhabditis* Genetics Center (CGC).

Plasmid construction

Plasmids were constructed using Gibson Assembly (Gibson et al., 2009). Briefly, the GFP nanobody vhhGFP4 fragment was PCR amplified from pcDNA3_NSlmb-vhhGFP4 (Addgene # 35579); the ZIF-1 genomic DNA (from ATG to TAA) and tissue-specific promoters were PCR amplified from N2 genomic DNA; the operon linker, mCherry::Histone H2b reporter and tbb-2 3′UTR were amplified from a previous construct in the lab (pOD1248); and the MosSCI targeting vector backbone was amplified from pCFJ151 (Frøkjær-Jensen et al., 2008). PCR primers were designed so that neighboring DNA fragments in the same construct had at least 20 bp overlap at each junction. Equimolar DNA fragment mixture (5 µl) was mixed with 15 µl of 1.33× home-made Gibson Assembly mix [133 mM Tris-HCl (pH 7.5), 267 µM each dNTP, 1.33 mM NAD, 6.67% PEG 8000, 13.3 mM $MgCl_2$, 13.3 mM DTT, 5.33 U/ml Epicentre T5 exonuclease, 33.3 U/ml Phusion high-fidelity DNA polymerase and 5.33 U/µl Taq DNA ligase], and incubated at 50°C for 1 h before 5-10 µl of the reaction was used for transformation. The DEG plasmid constructs along with complete sequences and maps have been deposited in Addgene by K.O. (Plasmid IDs 89357, 89366, 89367, 89368 and 89369).

Laser axotomy and light microscopy

Laser axotomy was performed as described previously (Chen et al., 2011). Images in Fig. 1B and Fig. S1A were acquired using an inverted Zeiss Axio Observer Z1 system equipped with AxioVision software, a Yokogawa spinning-disk confocal head (CSU-X1), a 63×1.40 NA Plan Apochromat lens (Zeiss) and a Hamamatsu ORCA-ER camera (Model C4742-95-12ERG, Hamamatsu Photonics). Images in Figs 1C,D, 5A and Fig. S1B were acquired on the same system using an EMCCD camera (QuantEM:512SC, Photometrics). Images in Fig. 2, Figs S1C-D and S2 were acquired using a Nikon TE2000-E inverted microscope equipped with Andor iQ2 software, a Yokogawa spinning-disk confocal head (CSU-10), a 60×1.40 NA Plan Apochromat lens (Nikon, Tokyo, Japan) and an EMCCD camera (iXon DV887ECS-BV, Andor Technology). Images in Fig. 3A,C, Fig. 5B, Fig. S3, and Movies 1-2 were acquired using a CV1000 spinning disk confocal system (Yokogawa Electric) maintained in a 16°C temperature-controlled room, using a 60×1.35NA U-PlanApo objective and a 512×512 EM-CCD camera (Hamamatsu). Images in Fig. 4D,E and Fig. S4 were acquired using Zeiss LSM510 (Fig. 4D) and LSM710 (Fig. 4E and Fig. S4; Zeiss Plan Apochromat 63×1.4 NA oil DIC objective) confocal microscopes controlled by ZEN software (Zeiss). Images in Fig. 5E were acquired using the DinoEye eyepiece camera (AM7023B, Dino-Lite) mounted on a Nikon SMZ800 dissection scope using the DinoXcope software (Dino-Lite).

Image analysis

Image analysis was first performed with Fiji (Image J) in a semi-automated manner aided by customized macros. Either a box or a line was made inside or across the region of interest to measure raw GFP intensities. Raw measurements were analyzed using customized Python scripts to compute final values. For details, see Fig. S1 and the supplementary Materials and Methods.

Acknowledgements

The GFP nanobody vhhGFP4 was cloned from pcDNA3_NSlmb-vhhGFP4, a gift from Markus Affolter (University of Basel, Switzerland) (Addgene plasmid #35579). We thank Kentaro Noma and Yishi Jin for sharing the GFP::DLK-1 transgene prior to publication. We thank the *Caenorhabditis* Genetics Center for strains, and members of the Chisholm lab and the Oegema Desai labs for helpful discussions.

Competing interests

The authors declare no competing or financial interests.

Author contributions

Conceptualization: S.W., N.H.T., A.D.C., A.D., K.O.; Methodology: S.W.; Formal analysis: S.W., N.H.T., P.L.-G.; Investigation: S.W., N.H.T., P.L.-G., Z.Z., D.K.C., B.P.; Writing - original draft: S.W., A.D., K.O.; Writing - review & editing: S.W., N.H.T., A.D.C., A.D., K.O.; Visualization: S.W., N.H.T.; Supervision: A.D.C., K.O.; Project administration: A.D.C., A.D., K.O.; Funding acquisition: A.D.C., A.D., K.O.

Funding

This work was supported by grants from the National Institutes of Health to K.O. (GM074207) and A.D.C. (NS093588). A.D. and K.O. receive salary and other support from the Ludwig Institute for Cancer Research. Deposited in PMC for release after 12 months.

Supplementary information

Supplementary information available online at
http://dev.biologists.org/lookup/doi/10.1242/dev.150094.supplemental

References

Armenti, S. T., Lohmer, L. L., Sherwood, D. R. and Nance, J. (2014). Repurposing an endogenous degradation system for rapid and targeted depletion of C. elegans proteins. *Development* **141**, 4640-4647.

Caussinus, E., Kanca, O. and Affolter, M. (2012). Fluorescent fusion protein knockout mediated by anti-GFP nanobody. *Nat. Struct. Mol. Biol.* **19**, 117-121.

Chen, L., Wang, Z., Ghosh-Roy, A., Hubert, T., Yan, D., O'Rourke, S., Bowerman, B., Wu, Z., Jin, Y. and Chisholm, A. D. (2011). Axon regeneration pathways identified by systematic genetic screening in C. elegans. *Neuron* **71**, 1043-1057.

Collet, J., Spike, C. A., Lundquist, E. A., Shaw, J. E. and Herman, R. K. (1998). Analysis of osm-6, a gene that affects sensory cilium structure and sensory neuron function in Caenorhabditis elegans. *Genetics* **148**, 187-200.

Deppe, U., Schierenberg, E., Cole, T., Krieg, C., Schmitt, D., Yoder, B. and von Ehrenstein, G. (1978). Cell lineages of the embryo of the nematode Caenorhabditis elegans. *Proc. Natl. Acad. Sci. USA* **75**, 376-380.

DeRenzo, C., Reese, K. J. and Seydoux, G. (2003). Exclusion of germ plasm proteins from somatic lineages by cullin-dependent degradation. *Nature* **424**, 685-689.

Dickinson, D. J., Ward, J. D., Reiner, D. J. and Goldstein, B. (2013). Engineering the Caenorhabditis elegans genome using Cas9-triggered homologous recombination. *Nat. Methods* **10**, 1028-1034.

Dickinson, D. J., Pani, A. M., Heppert, J. K., Higgins, C. D. and Goldstein, B. (2015). Streamlined genome engineering with a self-excising drug selection cassette. *Genetics* **200**, 1035-1049.

Feldman, J. L. and Priess, J. R. (2012). A role for the centrosome and PAR-3 in the hand-off of MTOC function during epithelial polarization. *Curr. Biol.* **22**, 575-582.

Fire, A. and Waterston, R. H. (1989). Proper expression of myosin genes in transgenic nematodes. *EMBO J.* **8**, 3419-3428.

Frøkjær-Jensen, C., Davis, M. W., Hopkins, C. E., Newman, B. J., Thummel, J. M., Olesen, S.-P., Grunnet, M. and Jorgensen, E. M. (2008). Single-copy insertion of transgenes in Caenorhabditis elegans. *Nat. Genet.* **40**, 1375-1383.

Fukushige, T., Hawkins, M. G. and McGhee, J. D. (1998). The GATA-factor elt-2 is essential for formation of the Caenorhabditis elegans intestine. *Dev. Biol.* **198**, 286-302.

Gibson, D. G., Young, L., Chuang, R.-Y., Venter, J. C., Hutchison, C. A. and Smith, H. O. (2009). Enzymatic assembly of DNA molecules up to several hundred kilobases. *Nat. Methods* **6**, 343-345.

Hammarlund, M., Nix, P., Hauth, L., Jorgensen, E. M. and Bastiani, M. (2009). Axon regeneration requires a conserved MAP kinase pathway. *Science* **323**, 802-806.

Hannak, E., Oegema, K., Kirkham, M., Gönczy, P., Habermann, B. and Hyman, A. A. (2002). The kinetically dominant assembly pathway for centrosomal asters in Caenorhabditis elegans is gamma-tubulin dependent. *J. Cell Biol.* **157**, 591-602.

Holland, A. J., Fachinetti, D., Han, J. S. and Cleveland, D. W. (2012). Inducible, reversible system for the rapid and complete degradation of proteins in mammalian cells. *Proc. Natl. Acad. Sci. USA* **109**, E3350-E3357.

Huang, T., Kuersten, S., Deshpande, A. M., Spieth, J., MacMorris, M. and Blumenthal, T. (2001). Intercistronic region required for polycistronic pre-mRNA processing in Caenorhabditis elegans. *Mol. Cell. Biol.* **21**, 1111-1120.

Hubbard, E. J. A. (2014). FLP/FRT and Cre/lox recombination technology in C. elegans. *Methods* **68**, 417-424.

McGhee, J. D., Sleumer, M. C., Bilenky, M., Wong, K., McKay, S. J., Goszczynski, B., Tian, H., Krich, N. D., Khattra, J., Holt, R. A. et al. (2007). The ELT-2 GATA-factor and the global regulation of transcription in the C. elegans intestine. *Dev. Biol.* **302**, 627-645.

Nishimura, K., Fukagawa, T., Takisawa, H., Kakimoto, T. and Kanemaki, M. (2009). An auxin-based degron system for the rapid depletion of proteins in nonplant cells. *Nat. Methods* **6**, 917-922.

Development (2017) 144, 2694-2701 doi:10.1242/dev.150094

Paix, A., Schmidt, H. and Seydoux, G. (2016). Cas9-assisted recombineering in C. elegans: genome editing using in vivo assembly of linear DNAs. *Nucleic Acids Res.* **44**, e128.

Qadota, H., Inoue, M., Hikita, T., Köppen, M., Hardin, J. D., Amano, M., Moerman, D. G. and Kaibuchi, K. (2007). Establishment of a tissue-specific RNAi system in C. elegans. *Gene* **400**, 166-173.

Reese, K. J., Dunn, M. A., Waddle, J. A. and Seydoux, G. (2000). Asymmetric segregation of PIE-1 in C. elegans is mediated by two complementary mechanisms that act through separate PIE-1 protein domains. *Mol. Cell* **6**, 445-455.

Rothbauer, U., Zolghadr, K., Tillib, S., Nowak, D., Schermelleh, L., Gahl, A., Backmann, N., Conrath, K., Muyldermans, S., Cardoso, M. C. et al. (2006). Targeting and tracing antigens in live cells with fluorescent nanobodies. *Nat. Methods* **3**, 887-889.

Shaner, N. C., Lambert, G. G., Chammas, A., Ni, Y., Cranfill, P. J., Baird, M. A., Sell, B. R., Allen, J. R., Day, R. N., Israelsson, M. et al. (2013). A bright monomeric green fluorescent protein derived from Branchiostoma lanceolatum. *Nat. Methods* **10**, 407-409.

Shen, Z., Zhang, X., Chai, Y., Zhu, Z., Yi, P., Feng, G., Li, W. and Ou, G. (2014). Conditional knockouts generated by engineered CRISPR-Cas9 endonuclease reveal the roles of coronin in C. elegans neural development. *Dev. Cell* **30**, 625-636.

Strome, S., Powers, J., Dunn, M., Reese, K., Malone, C. J., White, J., Seydoux, G. and Saxton, W. (2001). Spindle dynamics and the role of gamma-tubulin in early Caenorhabditis elegans embryos. *Mol. Biol. Cell* **12**, 1751-1764.

Wang, S., Wu, D., Quintin, S., Green, R. A., Cheerambathur, D. K., Ochoa, S. D., Desai, A. and Oegema, K. (2015). NOCA-1 functions with γ-tubulin and in parallel to Patronin to assemble non-centrosomal microtubule arrays in C. elegans. *Elife* **4**, e08649.

Wu, Q., Ploegh, H. L. and Truttmann, M. C. (2017). Hepta-Mutant Staphylococcus aureus Sortase A (SrtA7m) as a Tool for in Vivo Protein Labeling in Caenorhabditis elegans. *ACS Chem. Biol.* **12**, 664-673.

Yan, D., Wu, Z., Chisholm, A. D. and Jin, Y. (2009). The DLK-1 kinase promotes mRNA stability and local translation in C. elegans synapses and axon regeneration. *Cell* **138**, 1005-1018.

Zhang, L., Ward, J. D., Cheng, Z. and Dernburg, A. F. (2015). The auxin-inducible degradation (AID) system enables versatile conditional protein depletion in C. elegans. *Development* **142**, 4374-4384.

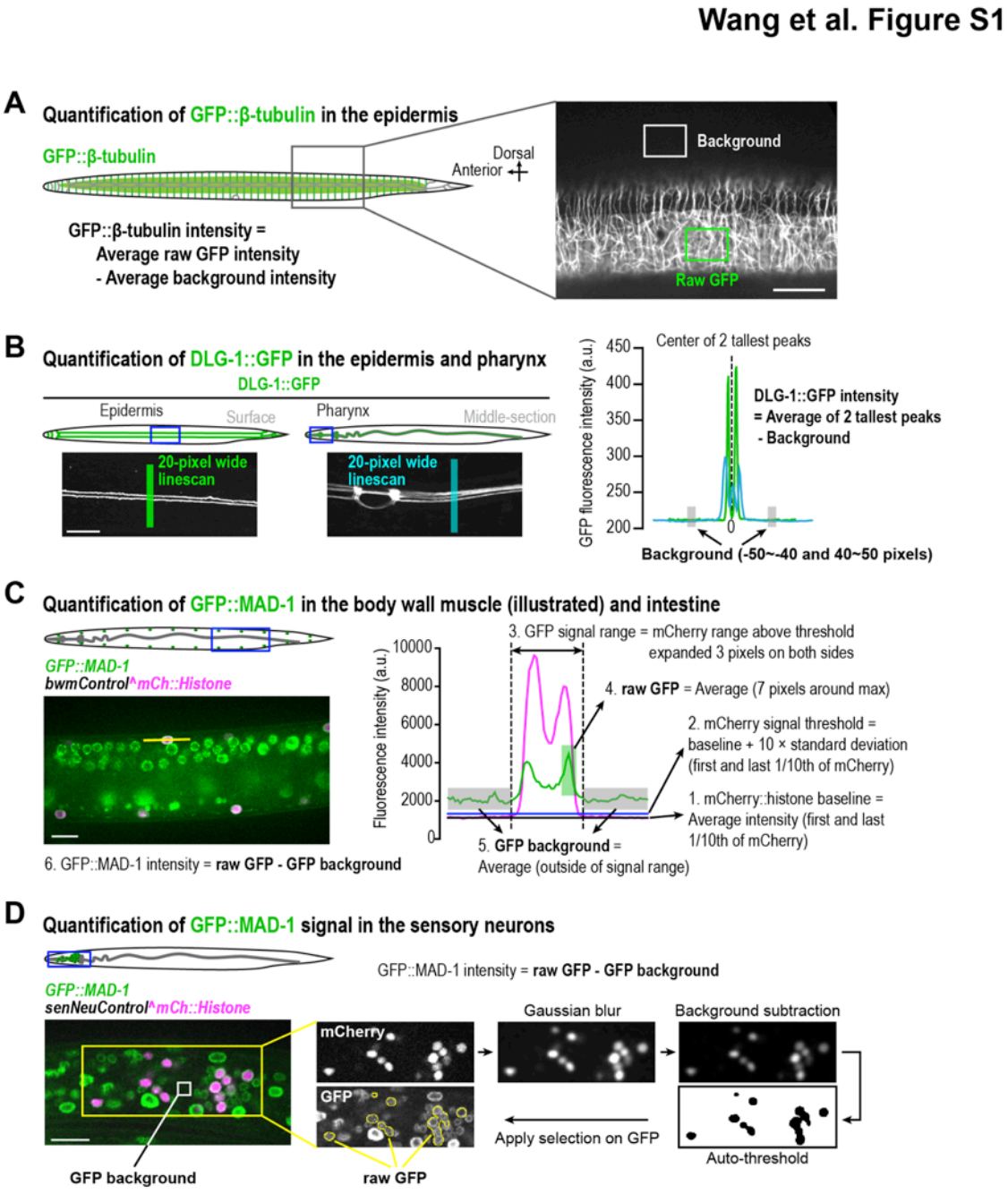

Fig. S1. Quantification methods. (**A**) Left: schematic illustrating the imaged area. Right: fluorescence confocal images of L3 stage worms expressing GFP::β-tubulin. Boxes mark the regions where background or raw GFP signals were measured. (**B**) Left: schematics and fluorescence confocal images of late L4 stage worms expressing

DLG-1::GFP. Green and cyan lines on the images mark where fluorescence profiles were recorded. Right: plot of DLG-1::GFP fluorescence intensity profiles along the lines in the left image. Center of the line scan profile is defined as the midpoint between the two tallest peaks. The signals 40-50 pixels away from the profile center on both sides are averaged and taken as the background. The GFP intensity is measured as the averaged intensity of the tallest 2 peaks after subtracting the background. (**C**) Left: schematic and fluorescence confocal image of a L3 stage worm expressing GFP::MAD-1. Right: plot of GFP::MAD-1 and mCherry::Histone fluorescence intensity profiles along the line in the left image. The “signal range” is first defined using the mCherry::Histone profile (steps 1~3). The “raw GFP” is calculated by averaging the intensity of 7 pixels surrounding the maximum GFP intensity within the “signal range” (step 4). The “GFP background” is defined as the average intensity of the GFP profile outside of the “signal range” (step 5). The GFP intensity is calculated by subtracting the “GFP background” from the “raw GFP” intensity (step 6). (**D**) Left: schematic and fluorescence confocal image of a L3 stage worm expressing GFP::MAD-1. Right: intermediate images illustrating the semi-automatic measurement of GFP::MAD-1 intensity in mCherry::Histone positive nuclei (sensory neurons). The mCherry::Histone image is smoothed, background-subtracted and applied auto-threshold to generate a mask of the region of interest (ROI). GFP signal within the ROI is averaged to get the raw GFP intensity. GFP background is measured by averaging the GFP signal in a small box inside the worm but outside of any nuclei. GFP intensity is calculated by subtracting the “GFP background” from the “raw GFP” intensity. Scale bars, 10 μm.

Wang et al. Figure S2

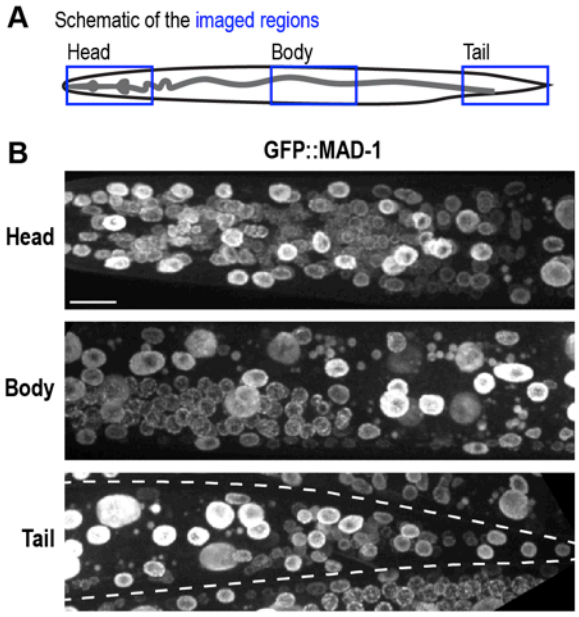

Fig. S2. GFP::MAD-1 is widely expressed. (**A**) Schematic of imaged regions. (**B**) Maximum intensity projection of 20 fluorescence confocal images acquired at 1 µm z-steps of L3 stage worms expressing endogenously tagged GFP::MAD-1. White dashed line in the bottom image outlines the worm boundary. Scale bar, 10 µm.

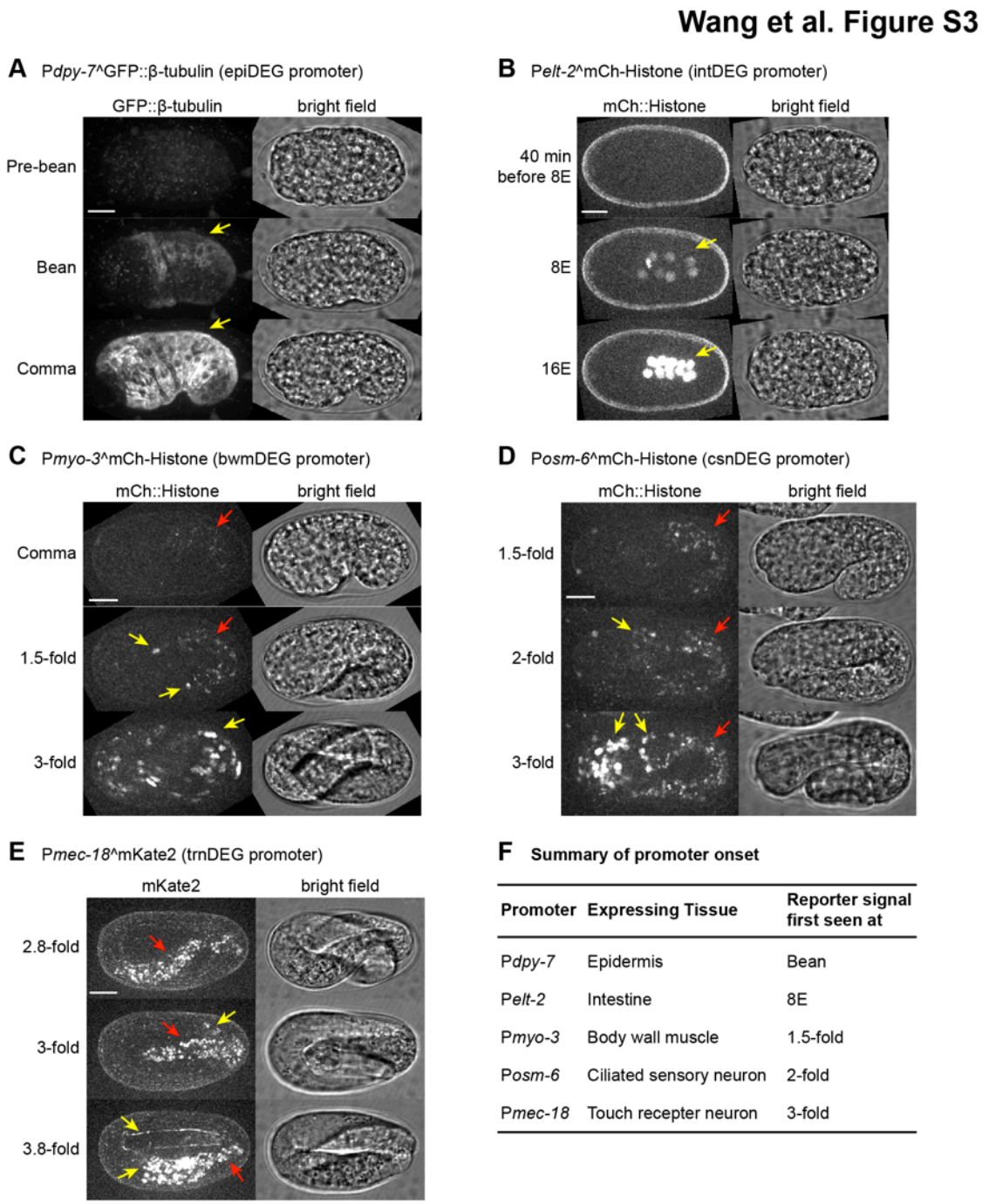

Promoter	Expressing Tissue	Reporter signal first seen at
P*dpy-7*	Epidermis	Bean
P*elt-2*	Intestine	8E
P*myo-3*	Body wall muscle	1.5-fold
P*osm-6*	Ciliated sensory neuron	2-fold
P*mec-18*	Touch recepter neuron	3-fold

Fig. S3. Onset of promoters used to drive expression of the GFP nanobody::ZIF-1 fusion. (**A-E**) Maximum intensity projections of confocal fluorescence images (*left*) or bright field images (*right*) of *C. elegans* embryos at indicated stages. (**F**) Summary of the stage when each of the five promoters used to drive expression of the GFP nanobody::ZIF-1 fusion turn on. Yellow arrows point to the reporter signal and red

arrows point to autofluorescence signals from the embryonic intestine. Scale bars, 10 μm.

Wang et al. Figure S4

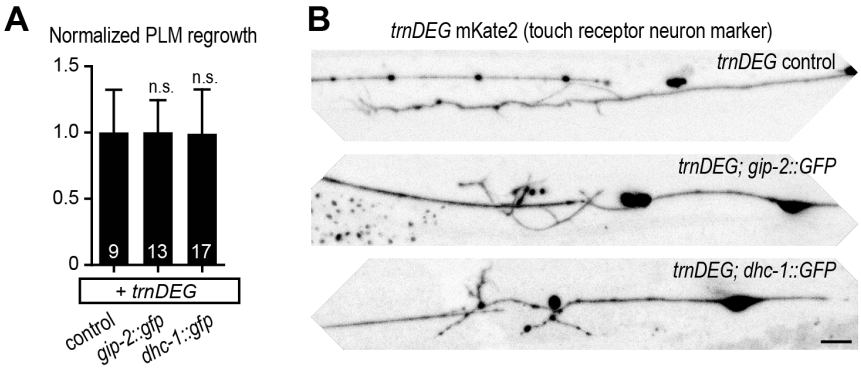

Fig. S4. DHC-1 and GIP-2 may not be required for axon regeneration in touch receptor neurons. (**A**) Plot of normalized touch receptor neuron (PLM) regrowth at 24 hours post laser axotomy of worms with indicated genotypes. The number in each bar is the number of analyzed worms. (**B**) Inverted grayscale images of the touch neuron (PLM) axon from worms with indicated genotypes. Note that both *gip-2::GFP* and *dhc-1::GFP* are endogenously tagged. Statistics, One-way ANOVA with Bonferroni's post test. Data are shown as mean ± s.d.. n.s., not significant. Scale bar, 10 μm.

Movies

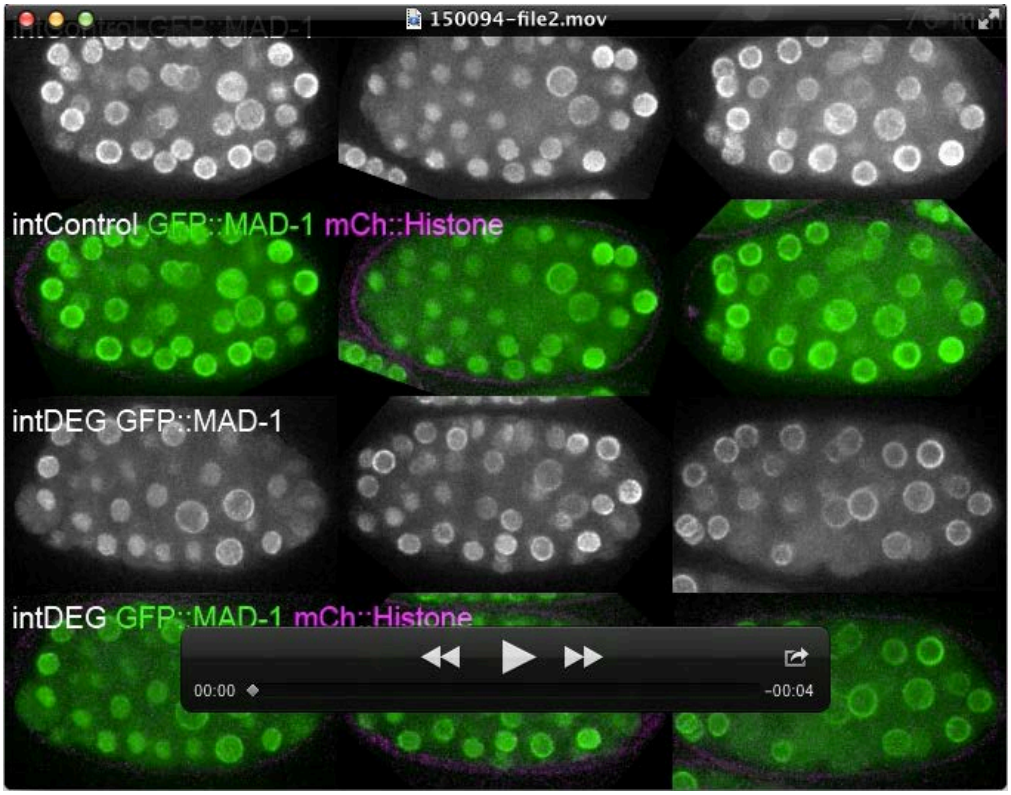

Movie 1. GFP::MAD-1 degradation in the embryonic intestine is rapid and penetrant. Timelapse fluorescence confocal microscopy was used to acquire images of developing *C. elegans* embryos expressing GFP::MAD-1 (*in situ*-tagged) together with either the *intControl* (***top two rows***) or *intDEG* (***bottom two rows***) transgene cassettes, both of which express the mCherry::Histone reporter. An 18-plane z-stack (2 µm step size) was acquired every 4 minutes. Images show a maximum intensity projection of the three middle slices. Playback is 1920× realtime.

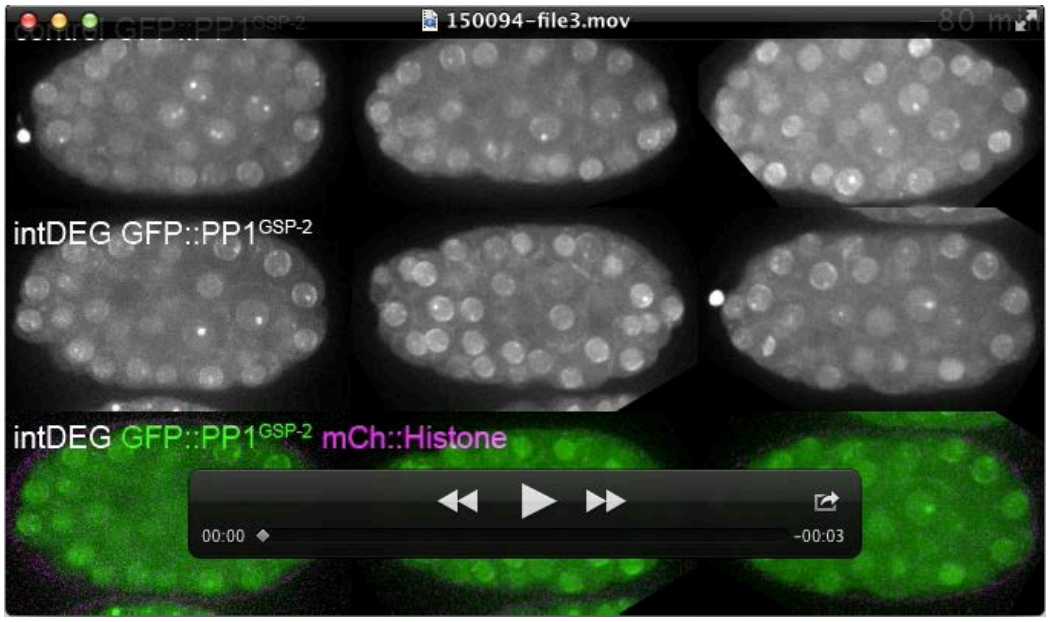

Movie 2. GFP::PP1^{GSP-2} degradation in the embryonic intestine is rapid and penetrant. Timelapse fluorescence confocal microscopy was used to acquire images of developing *C. elegans* embryos expressing GFP::PP1^{GSP-2} (*in situ*-tagged) in the absence (***top row***) or presence (***middle and bottom rows***) of the *intDEG* transgene cassette, which expresses the mCherry::Histone reporter. An 18-plane z-stack (2 µm step size) was acquired every 4 minutes. Images show a maximum intensity projection of the three middle slices. Playback is 1920× realtime.

Table S1. Promoters for tissue-specific expression of the GFP nanobody::ZIF-1 fusion and tested target GFP fusions

Tissue	Promoter	Strain #	*Strain name	Tested GFP fusions
Epidermis	P*dpy-7*	OD2442	epiDEG	GIP-2::GFP, GFP::β-tubulin^{TBB-2}, DLG-1::GFP, GFP::MAD-1
Intestine	P*elt-2*	OD2768	intDEG	GFP::MAD-1, GFP::PP1^{GSP-2}, GIP-2::GFP, PLK-1::sGFP
Body wall muscle	P*myo-3*	OD2770	bwmDEG	GFP::MAD-1
Ciliated sensory neurons	P*osm-6*	OD2772	csnDEG	GFP::MAD-1
Touch receptor neurons	P*mec-18*	OD2984	trnDEG	GFP::DLK-1, GIP-2::GFP, DHC-1::GFP

*These “DEG” strains are available from the Caenorhabditis Genetics Center.

SUPPLEMENTAL MATERIALS AND METHODS

C. elegans strains used in this study

Strain number	Genotype
Fig. 1	
OD1741	*ltSi570[pOD1527/pSW232; Pdpy-7::GFP-tbb-2::mCherry-his-11; cb-unc-119(+)]I; unc-119(ed3)III*
OD2442 (epiDEG)	*ltSi794[pOD1988/pSW302; Pdpy-7::vhhGFP4::ZIF-1::unc-54_3'UTR; cb-unc-119(+)]II; unc-119(ed3)III*
OD2507	*ltSi570[pOD1527/pSW232; Pdpy-7::GFP-tbb-2::mCherry-his-11; cb-unc-119(+)]I; ltSi794[pOD1988/pSW302; Pdpy-7::vhhGFP4::ZIF-1::unc-54_3'UTR; cb-unc-119(+)]II; unc-119(ed3)III?*
OD961	*ltSi249[pOD1274/pSW098; Pdlg-1delta7::dlg-1-GFP::unc-54-3'UTR; cb-unc-119(+)]I*
OD2534	*ltSi249[pOD1274/pSW098; Pdlg-1delta7::dlg-1-GFP::unc-54-3'UTR; cb-unc-119(+)]I; ltSi794[pOD1988/pSW302; Pdpy-7::vhhGFP4::ZIF-1::unc-54_3'UTR; cb-unc-119(+)]II; unc-119(ed3)III?*
OD2906	*mad-1(lt39[gfp::tev::loxP::3xFlag::mad-1])V*
OD2965	*ltSi794[pOD1988/pSW302; Pdpy-7::vhhGFP4::ZIF-1::unc-54_3'UTR; cb-unc-119(+)]II; unc-119(ed3)III?; mad-1(lt39[gfp::tev::loxP::3xFlag::mad-1])V*
Fig. 2	
OD2768 (intDEG)	*ltSi910[pOD2044/pSW378; Pelt-2::vhhGFP4::ZIF-1::operon-linker::mCherry::histone::tbb-2_3'UTR; cb-unc-119(+)]II; unc-119(ed3)III*
OD2769 (intControl)	*ltSi911[pOD2045/pSW379; Pelt-2::ZIF-1::operon-linker::mCherry::histone::tbb-2_3'UTR; cb-unc-119(+)]II; unc-119(ed3)III*
OD2770 (bwmDEG)	*ltSi912[pOD2046/pSW380; Pmyo-3::vhhGFP4::ZIF-1::operon-linker::mCherry::histone::tbb-2_3'UTR; cb-unc-119(+)]II; unc-119(ed3)III*
OD2771 (bwmControl)	*ltSi913[pOD2047/pSW381; Pmyo-3::ZIF-1::operon-linker::mCherry::histone::tbb-2_3'UTR; cb-unc-119(+)]II; unc-119(ed3)III*
OD2772 (csnDEG)	*ltSi914[pOD2048/pSW382; Posm-6::vhhGFP4::ZIF-1::operon-linker::mCherry::histone::tbb-2_3'UTR; cb-unc-119(+)]II; unc-119(ed3)III*

OD2773 (csnControl)	*ltSi915[pOD2049/pSW383; Posm-6::ZIF-1::operon-linker::mCherry::histone::tbb-2_3'UTR; cb-unc-119(+)]II; unc-119(ed3)III*
OD2967	*ltSi910[pOD2044/pSW378; Pelt-2::vhhGFP4::ZIF-1::operon-linker::mCherry::histone::tbb-2_3'UTR; cb-unc-119(+)]II; unc-119(ed3)III?; mad-1(lt39[gfp::tev::loxP::3xFlag::mad-1])V*
OD2968	*ltSi912[pOD2046/pSW380; Pmyo-3::vhhGFP4::ZIF-1::operon-linker::mCherry::histone::tbb-2_3'UTR; cb-unc-119(+)]II; unc-119(ed3)III?; mad-1(lt39[gfp::tev::loxP::3xFlag::mad-1])V*
OD2969	*ltSi914[pOD2048/pSW382; Posm-6::vhhGFP4::ZIF-1::operon-linker::mCherry::histone::tbb-2_3'UTR; cb-unc-119(+)]II; unc-119(ed3)III?; mad-1(lt39[gfp::tev::loxP::3xFlag::mad-1])V*
OD3055	*ltSi911[pOD2045/pSW379; Pelt-2::ZIF-1::operon-linker::mCherry::histone::tbb-2_3'UTR; cb-unc-119(+)]II; unc-119(ed3)III?; mad-1(lt39[gfp::tev::loxP::3xFlag::mad-1])V*
OD3056	*ltSi913[pOD2047/pSW381; Pmyo-3::ZIF-1::operon-linker::mCherry::histone::tbb-2_3'UTR; cb-unc-119(+)]II; unc-119(ed3)III?; mad-1(lt39[gfp::tev::loxP::3xFlag::mad-1])V*
OD3057	*ltSi915[pOD2049/pSW383; Posm-6::ZIF-1::operon-linker::mCherry::histone::tbb-2_3'UTR; cb-unc-119(+)]II; unc-119(ed3)III?; mad-1(lt39[gfp::tev::loxP::3xFlag::mad-1])V*
Fig. 3	
OD2906	*mad-1(lt39[gfp::tev::loxP::3xFlag::mad-1])V*
OD2967	*ltSi910[pOD2044/pSW378; Pelt-2::vhhGFP4::ZIF-1::operon-linker::mCherry::histone::tbb-2_3'UTR; cb-unc-119(+)]II; unc-119(ed3)III?; mad-1(lt39[gfp::tev::loxP::3xFlag::mad-1])V*
OD3055	*ltSi911[pOD2045/pSW379; Pelt-2::ZIF-1::operon-linker::mCherry::histone::tbb-2_3'UTR; cb-unc-119(+)]II; unc-119(ed3)III?; mad-1(lt39[gfp::tev::loxP::3xFlag::mad-1])V*
OD2866	*gsp-2(lt27[GFP::gsp-2])III*
OD2970	*gsp-2(lt27[GFP::gsp-2])III; ltSi910[pOD2044/pSW378; Pelt-2::vhhGFP4::ZIF-1::operon-linker::mCherry::histone::tbb-2_3'UTR; cb-unc-119(+)]II; unc-119(ed3)III?*
Fig. 4	
CZ10969	*muIs32[Pmec-7::GFP]II*

CZ20287	*muIs32[Pmec-7::GFP]II; juSi163[Prgef-1::GFP::DLK-1L]III; unc-119(ed3)III*
CZ12095	*dlk-1(tm4024)I; muIs32[Pmec-7::GFP]II; unc-119(ed3)III*
CZ20289	*dlk-1(tm4024)I; muIs32[Pmec-7::GFP]II; juSi163[Prgef-1::GFP::DLK-1L]III; unc-119(ed3)III*
OD2984 (trnDEG)	*ltSi953[pOD2087/pSW408; Pmec-18::vhhGFP4::ZIF-1::operon-linker::mKate2::tbb-2_3'UTR; cb-unc-119(+)]II; unc-119(ed3)III*
CZ24276	*ltSi953[pOD2087/pSW408; Pmec-18::vhhGFP4::ZIF-1::operon-linker::mKate2::tbb-2_3'UTR; cb-unc-119(+)]II; juSi163[Prgef-1::GFP::DLK-1L]III; unc-119(ed3)III?*
CZ24275	*dlk-1(tm4024)I; ltSi953[pOD2087/pSW408; Pmec-18::vhhGFP4::ZIF-1::operon-linker::mKate2::tbb-2_3'UTR; cb-unc-119(+)]II; unc-119(ed3)III?*
CZ24277	*dlk-1(tm4024)I; ltSi953[pOD2087/pSW408; Pmec-18::vhhGFP4::ZIF-1::operon-linker::mKate2::tbb-2_3'UTR; cb-unc-119(+)]II; juSi163[Prgef-1::GFP::DLK-1L]III; unc-119(ed3)III?*
Fig. 5	
N2	*wild type (ancestral)*
OD2509	*gip-2(lt19[gip-2::GFP]::loxP::cb-unc-119(+)::loxP)I; unc-119(ed3)III*
OD2768	*ltSi910[pOD2044/pSW378; Pelt-2::vhhGFP4::ZIF-1::operon-linker::mCherry::histone::tbb-2_3'UTR; cb-unc-119(+)]II; unc-119(ed3)III*
OD2769	*ltSi911[pOD2045/pSW379; Pelt-2::ZIF-1::operon-linker::mCherry::histone::tbb-2_3'UTR; cb-unc-119(+)]II; unc-119(ed3)III*
OD2778	*gip-2(lt19[gip-2::GFP]::loxP::cb-unc-119(+)::loxP)I; ltSi910[pOD2044/pSW378; Pelt-2::vhhGFP4::ZIF-1::operon-linker::mCherry::histone::tbb-2_3'UTR; cb-unc-119(+)]II; unc-119(ed3)III?*
OD2779	*gip-2(lt19[gip-2::GFP]::loxP::cb-unc-119(+)::loxP)I; ltSi911[pOD2045/pSW379; Pelt-2::ZIF-1::operon-linker::mCherry::histone::tbb-2_3'UTR; cb-unc-119(+)]II; unc-119(ed3)III?*
OD2425	*plk-1(lt18[plk-1::sGFP]::loxp)III*
OD3657	*ltSi910[pOD2044/pSW378; Pelt-2::vhhGFP4::ZIF-1::operon-linker::mCherry::histone::tbb-2_3'UTR; cb-unc-119(+)]II; unc-*

	119(ed3)III?; plk-1(lt18[plk-1::sGFP]::loxp)III
OD3658	*ltSi911[pOD2045/pSW379; Pelt-2::ZIF-1::operon-linker::mCherry::histone::tbb-2_3'UTR; cb-unc-119(+)]II; unc-119(ed3)III?; plk-1(lt18[plk-1::sGFP]::loxp)III*
Fig. S1	
OD1741	*ltSi570[pOD1527/pSW232; Pdpy-7::GFP-tbb-2::mCherry-his-11; cb-unc-119(+)]I; unc-119(ed3)III*
OD961	*ltSi249[pOD1274/pSW098; Pdlg-1delta7::dlg-1-GFP::unc-54-3'UTR; cb-unc-119(+)]I*
OD3056	*ltSi913[pOD2047/pSW381; Pmyo-3::ZIF-1::operon-linker::mCherry::histone::tbb-2_3'UTR; cb-unc-119(+)]II; unc-119(ed3)III?; mad-1(lt39[gfp::tev::loxP::3xFlag::mad-1])V*
OD3057	*ltSi915[pOD2049/pSW383; Posm-6::ZIF-1::operon-linker::mCherry::histone::tbb-2_3'UTR; cb-unc-119(+)]II; unc-119(ed3)III?; mad-1(lt39[gfp::tev::loxP::3xFlag::mad-1])V*
Fig. S2	
OD3055	*ltSi911[pOD2045/pSW379; Pelt-2::ZIF-1::operon-linker::mCherry::histone::tbb-2_3'UTR; cb-unc-119(+)]II; unc-119(ed3)III?; mad-1(lt39[gfp::tev::loxP::3xFlag::mad-1])V*
OD3057	*ltSi915[pOD2049/pSW383; Posm-6::ZIF-1::operon-linker::mCherry::histone::tbb-2_3'UTR; cb-unc-119(+)]II; unc-119(ed3)III?; mad-1(lt39[gfp::tev::loxP::3xFlag::mad-1])V*
Fig. S3	
OD1741	*ltSi570[pOD1527/pSW232; Pdpy-7::GFP-tbb-2::mCherry-his-11; cb-unc-119(+)]I; unc-119(ed3)III*
OD2967	*ltSi910[pOD2044/pSW378; Pelt-2::vhhGFP4::ZIF-1::operon-linker::mCherry::histone::tbb-2_3'UTR; cb-unc-119(+)]II; unc-119(ed3)III?; mad-1(lt39[gfp::tev::loxP::3xFlag::mad-1])V*
OD2770 (bwmDEG)	*ltSi912[pOD2046/pSW380; Pmyo-3::vhhGFP4::ZIF-1::operon-linker::mCherry::histone::tbb-2_3'UTR; cb-unc-119(+)]II; unc-119(ed3)III*
OD2772 (csnDEG)	*ltSi914[pOD2048/pSW382; Posm-6::vhhGFP4::ZIF-1::operon-linker::mCherry::histone::tbb-2_3'UTR; cb-unc-119(+)]II; unc-119(ed3)III*
OD2984 (trnDEG)	*ltSi953[pOD2087/pSW408; Pmec-18::vhhGFP4::ZIF-1::operon-linker::mKate2::tbb-2_3'UTR; cb-unc-119(+)]II; unc-119(ed3)III*

Fig. S4	
OD2984	*ltSi953[pOD2087/pSW408; Pmec-18::vhhGFP4::ZIF-1::operon-linker::mKate2::tbb-2_3'UTR; cb-unc-119(+)]II; unc-119(ed3)III*
CZ24092	*ltSi953[pOD2087/pSW408; Pmec-18::vhhGFP4::ZIF-1::operon-linker::mKate2::tbb-2_3'UTR; cb-unc-119(+)]II; gip-2(lt19[gip-2::GFP]::loxP::cb-unc-119(+)::loxP)I; unc-119(ed3)III?*
CZ24274	*ltSi953[pOD2087/pSW408; Pmec-18::vhhGFP4::ZIF-1::operon-linker::mKate2::tbb-2_3'UTR; cb-unc-119(+)]II; dhc-1(lt45[dhc-1::GFP]); unc-119(ed3)III?*

Image Analysis

Image analysis was first performed in FIJI (an Image J distribution), often in a semi-automated manner aided by customized Image J macros. Raw measurements from FIJI were then analyzed using custom Python scripts to compute the final values.

To quantify GFP fluorescence intensities in **Fig. 1B**, a 80×60 pixel box was drawn inside the epidermis region to measure the raw GFP intensity and a same-size box was drawn outside of the worm to measure background GFP intensity (**Fig. S1A**). Measured GFP intensity was the raw GFP intensity minus the background GFP intensity.

To quantify GFP fluorescence intensities in **Fig. 1C**, a 20-pixel wide line scan was made across the epithelial junctions in the epidermis or pharynx (**Fig. S1B**). The two tallest peaks were automatically identified using a custom python script. GFP intensity was taken as the average intensity of the two tallest peaks subtracting background GFP intensity, which was calculated as the average intensity in the region between −50 and −40 and between 40 and 50 pixels from the center of the two tallest peaks.

To quantify GFP fluorescence intensities in **Fig. 2B-C**, a 5-pixel wide line was made across the mCherry-Histone marked target nuclei in GFP and mCherry merged images and line scan values of both GFP::MAD-1 and mCherry::Histone were recorded (**Fig. S1C**). The first and last 1/10 of the mCherry::Histone intensities were averaged to obtain the mCherry::Histone baseline. The threshold for the mCherry signal was set at a value equal to the baseline plus 10 times of the baseline standard deviation. The range of mCherry signals above this threshold was expanded by 3 pixels on both sides to define the GFP signal range because mCherry-Histone only localizes inside the nucleus, whereas GFP::MAD-1 also localizes to the nuclear envelope. Raw GFP intensity was defined as the average of 7 pixels around the GFP maximum within the signal range, while background GFP intensity was defined as the average of all GFP values outside of the signal range. Measured GFP intensity was the raw GFP intensity minus the background GFP intensity. The average value of 5 nuclei from the same worm was plotted as the final GFP intensity.

To quantify the GFP fluorescence intensities in **Fig. 2D**, a box was drawn in the pharynx region to enclose the mCherry::Histone reporter signal. The mCherry::Histone channel was subject to Gaussian blur (sigma = 2 pixels), background subtraction (radius = 20 pixels, sliding paraboloid method) and auto threshold to generate a region of interest in the mCherry-Histone expressing area (**Fig. S1D**). The mean GFP intensity within this region of interest was taken as the raw GFP intensity. Background GFP signal was estimated by drawing a box inside the worm but outside of any nuclei (**Fig. S1D**). Measured GFP intensity was the raw GFP intensity minus the background GFP intensity.

To quantify the total per embryo GFP intensity shown in **Fig. 3B**, a polygon was drawn around the whole embryo at the first time frame of imaging on the maximum intensity projection of 3 middle slices. The mean GFP intensity and area inside the polygon selection were recorded as GFP_in and Area_in. The polygon selection was then enlarged by 2 pixels, whose mean GFP intensity and area were recorded as GFP_out and Area_out. Local background was calculated as GFP_BG = (GFP_out × Area_out - GFP_in × Area_in) / (Area_out - Area_in). Raw total intensity per embryo was calculated as GFP_raw = Area_in × (GFP_in - GFP_BG). Three N2 wild type embryos were measured using this method to estimate the embryo auto-fluorescence and this value was subtracted from GFP_raw to obtain GFP_total. In the end, all GFP_total were divided by the mean value of GFP_total of GFP::MAD-1 for plotting.

To quantify the GFP::PP1^{GSP-2} intensity shown in **Fig. 3D**, a polygon was drawn around the intestine area at each time point on the maximum intensity projection of the 3 middle slices that were selected based on the mCherry::Histone reporter intensity. The mean GFP intensity inside the polygon selection was taken as the raw GFP intensity, and the mean mCherry intensity inside this selection was taken as the raw mCherry intensity. To estimate the GFP background signal inside the embryo, the out-of-focus signal at the top and bottom of embryos were measured, and the background signal of the middle slice was calculated by linear interpolation using the top and bottom out-of-focus signals. To account for GFP signal bleaching over time, a polygon outside the intestine (toward the head region) was drawn and the mean intensity was recorded for all time slices. Normalized GFP intensity was calculated as: (raw GFP intensity - background GFP) / (mean GFP outside intestine - background GFP). The background

mCherry signal was estimated from N2 wild type control embryos (3300) and subtracted from the raw mCherry intensities. Normalized mCherry intensity was calculated as: (raw mCherry intensity - 3300) / (mCherry intensity at the last time point -3300). Normalized GFP and mCherry intensities were plotted on the same graph and shown in **Fig. 3D**.

To measure the PLM regrowth length shown in **Fig. 4C and Fig. S4A**, a segmented line was drawn to trace the regenerated axon in Image J, and the length of this segmented line was taken as the raw PLM regrowth length. For normalization, all the raw measurements were divided by the mean of the same-day control group, so the mean of the control group was always 1.

To quantify the intestinal GIP-2::GFP intensity shown in **Fig. 5C**, a 25-pixel wide line was drawn across the intestine midline in GFP and mCherry merged images and line scan values of both GFP::MAD-1 and mCherry::Histone were recorded for 7 middle slices. The first 1/4 of the mCherry::Histone intensities were averaged to obtain the mCherry::Histone baseline. The threshold for the mCherry signal was set at a value equal to the baseline plus 10 times of the baseline standard deviation. The range of mCherry signals above this threshold was defined as the GFP signal range. Raw GFP intensity was defined as the average of 9 middle pixels within the GFP signal range, while background GFP intensity was defined as the average of GFP values in the first 1/4 of the GFP line scan intensities. Measured GFP intensity was the raw GFP intensity minus the background GFP intensity. The maximum value of the 7 measured middle slices from the same embryo was plotted as the final GFP intensity.

To quantify the GFP::PP1^{GSP-2} intensity shown in **Fig. 5C**, the mCherry::Histone reporter was used as a land mark to choose the middle intestinal slice. The mCherry

channel was subject to Gaussian blur (sigma = 1 pixel), rolling ball based background subtraction (radius = 50 pixels) and auto threshold to generate a region of interest in the mCherry-Histone expressing area. This region was expanded by 2 pixels and shrunken back by 2 pixels to include the inter-nuclear space. The mean GFP intensity inside this selection was taken as the raw GFP intensity. To estimate the background signal inside the embryo, the out-of-focus signal at the top and bottom of embryos were measured, and the background signal of the middle slice was calculated by linear interpolation using the top and bottom out-of-focus signals. Measured GFP intensity was the raw GFP intensity minus the background GFP intensity.

The number of intestinal nuclei shown in **Fig. 5D** was counted in Image J using the multi-point tool by going through the z slices of mCherry::Histone reporter images. The body length in **Fig. 5E** was measured in Image J by drawing a segmented line to trace the worm body from its nose to tail.